

# **Structure Refinement Based on the Maximum-Entropy Method from Powder Diffraction Data**

Fujio Izumi and Ruben A. Dilanian

Advanced Materials Laboratory, National Institute for Materials Science,  
1-1 Namiki, Tsukuba, Ibaraki 305-0044, Japan

## ABSTRACT

A multipurpose pattern-fitting program RIETAN-2000, PRIMA for the maximum-entropy method (MEM), and VENUS for three-dimensional (3D) visualization of crystal structures and electron/nuclear densities were substantially combined to grow into an integrated system for MEM-based pattern fitting (MPF). In MPF, ‘observed’ structure factors,  $F_o$ (Rietveld), estimated after Rietveld analysis are at first analyzed by MEM to yield 3D electron/nuclear densities that are more or less biased in favor of a structural model in the Rietveld analysis. Then, we evaluate structure factors,  $F_c$ (MEM), by the Fourier transform of the densities and fit the whole powder pattern calculated from the  $F_c$ (MEM) data to the observed one to refine parameters irrelevant to the structure.  $F_o$ (w.p.f.) data resulting from the whole-

pattern fitting (w.p.f.) are analyzed again by MEM. MEM analysis and whole-pattern fitting are alternately repeated until  $R$  factors in the latter no longer decrease. These iterative processes make it possible to minimize the bias imposed by the structural model on final electron/nuclear densities. With this sophisticated methodology, crystal structures are represented not by structure parameters such as fractional coordinates and atomic displacement parameters but by 3D electron/nuclear densities. MPF is, therefore, capable of modeling static and dynamic disorder, chemical bonds, nonlocalized electrons, and anharmonic thermal motion more adequately than the conventional Rietveld method. Applications of MPF to structure refinements of several compounds from (synchrotron) X-ray and neutron powder diffraction data will be demonstrated, showing the excellent performance and effectiveness of MPF.

# 1. INTRODUCTION

Sakata *et al.* have been applying the maximum-entropy method (MEM) [1] to determination of electron and nuclear (strictly speaking, coherent-scattering length  $b_c$  [2]) densities from powder diffraction data [3,4]. Diffraction intensities scattered in the reciprocal space are converted into electron/nuclear densities filling the real space; that is, the densities are visualized in three dimensions. MEM can estimate structure factors of reflections in the high- $Q$  region excluded in the analysis of the powder diffraction data, which is favorable for improving the S/N ratio in the three-dimensional (3D) densities.

When dealing with compounds exhibiting heavily overlapping reflections, integrated intensities are often estimated on the basis of the result of Rietveld analysis [5]. In this procedure, the observed intensity at each point is apportioned in the ratio of profiles calculated from final parameters and summed up for each reflection. The resultant ‘observed’ structure factors are then analyzed by MEM to give 3D electron/nuclear densities in the unit cell. Unfortunately, ‘observed’ structure factors evaluated in this way are doubly biased towards the structural model because both phases and calculated integrated intensities used for the intensity partitioning are taken from the model [6].

We have been claiming that the above undesirable effect, which is overlooked or disregarded by Sakata *et al.*, should be overcome if only partially [7–10]. Even if the structural model in the Rietveld analysis from X-ray powder diffraction data is essentially correct, chemical bonding is hardly represented with structure parameters such as fractional coordinates and atomic displacement parameters. This is the main reason for the necessity of D synthesis in studies of electron densities by single-crystal X-ray diffraction. Refinement of isotropic atomic displacement parameters,  $U$ , in Rietveld analysis (anisotropic atomic displacement parameters,  $U_{ij}$ , cannot practically be refined from X-ray powder diffraction data) and that of a scale factor on the basis of the inadequate structural model will lower the accuracy of the ‘observed’ structure factors.

In this article, we will introduce our original technology named MEM-based pattern fitting (MPF) [7–10]. We have integrated a multipurpose pattern-

fitting program RIETAN-2000 [7–11], a MEM analysis program PRIMA [12] (formerly MEED developed by Kumazawa *et al.* [13]), and a 3D visualization program VENUS [14] to construct a system to refine crystal structures by MPF from powder diffraction data. With this MPF system, the bias imposed on final electron/nuclear densities can efficiently be reduced by running RIETAN and PRIMA alternately.

Several examples of MPF structure refinements from (synchrotron) X-ray and neutron powder diffraction data will be demonstrated to verify its high performance and effectiveness.

# 2. BACKGROUND

In single-crystal X-ray analysis, we often carry out difference (D) synthesis, *i.e.*, the inverse Fourier transform of differences, between observed structure factors,  $F_{ok}$ , and structure factors,  $F_{ck}$ , calculated from structure parameters:

$$\Delta F_k = F_{ok} - F_{ck}. \quad (1)$$

D synthesis is suitable for detecting subtle differences between real and modeled structures.

Two serious problems hinder the satisfactory application of D synthesis to powder diffraction data. One is the appearance of ‘ripples’ due to the termination effect even in D synthesis where Fourier coefficients with higher orders are regarded as negligible. This effect makes it difficult to extract physically meaningful residual distribution from D-synthesis maps. The other is difficulty in obtaining accurate observed structure factors,  $|F_{ok}|$ , owing to the collapse of the 3D reciprocal space onto the one-dimensional diffraction pattern.

In MEM analysis, no model function is fit to the observed pattern unlike Rietveld analysis using least-squares methods [5]; that is, we estimate density distribution whose information entropy is maximized within errors in observed diffraction data. Structural information contained in diffraction data is accordingly extracted by MEM and reflected on the 3D densities provided that the diffraction data have been measured in an appropriate way. Electron densities are calculated from  $F_{ok}$ ’s in Fourier synthesis. On the other hand, in MEM, we solve a kind of an inverse

problem where electron densities are determined prior to calculation of structure factors,  $F_{Mk}$ . The termination effect is, consequently, far less marked in MEM analysis than in Fourier synthesis. Further, the MEM can estimate structure factors of reflections in the high- $Q$  region excluded in the analysis of intensity data, as described earlier. MEM analysis, therefore, gives less noisy 3D densities than Fourier synthesis from a limited number of observed reflections.

The distribution of  $b_c$  is also determinable by the MEM analysis of neutron diffraction data. The term “nuclear density” may be substituted for “electron density” in subsequent general descriptions common to X-ray and neutron diffraction.

### 3. SUPER-FAST MEM ANALYSIS PROGRAM, PRIMA

Till lately, we had been utilizing MEED [13] for MEM analysis. MEED is, however, obsolete at present because of its sluggish speed. We have recently developed our own program PRIMA [12], the state of the art in MEM analysis of structure factors obtained experimentally by X-ray and neutron diffraction. PRIMA can determine 3D electron-density distribution from X-ray diffraction data and 3D nuclear-density distribution from neutron diffraction data. In the case of neutron diffraction, it can deal with compounds containing elements whose  $b_c$ 's are negative, *e.g.*, H, Li, Ti, and Mn [2]. PRIMA was written in Fortran 90, which enables us to create storage for allocatable arrays dynamically. It is thoroughly optimized for personal computers equipped with Intel Pentium 4 processors and operated with Microsoft Windows.

#### 3.1 Maximum-entropy equation

The general principle of MEM analysis is to find the maximum of the information entropy,  $S$ , under several constraints. There are a few variations of the MEM formalism [15–17]. Here, we will follow Collins's formalism [16] based on Jaynes's expression of the information entropy [18].

In MEM analysis of X-ray/neutron diffraction data, electron/nuclear densities are represented with those in pixels (parallelepipeds) whose numbers along

$a$ ,  $b$ , and  $c$  axes are  $N_a$ ,  $N_b$ , and  $N_c$ , respectively. Let  $N$  ( $= N_a N_b N_c$ ) be the total number of pixels in the unit cell,  $\rho_k$  the normalized density at the position  $\mathbf{r}_k$  in the 3D gridded space,  $\rho_k^*$  the density at  $\mathbf{r}_k$ , and  $\tau_k$  the normalized density at  $\mathbf{r}_k$  derived from prior information. Then,  $S$  is formulated as

$$S = - \sum_{k=1}^N \rho_k \ln \left( \frac{\rho_k}{\tau_k} \right) \quad (2)$$

with

$$\rho_k = \frac{\rho_k^*}{\sum_{k=1}^N \rho_k^*}. \quad (3)$$

$S$  is maximized by imposing the following three constraints:

$$\rho_k > 0, \quad (4)$$

$$C = \frac{1}{M} \sum_{j=1}^M \frac{|F_c(\mathbf{h}_j) - F_o(\mathbf{h}_j)|^2}{\sigma_j^2} = 1, \quad (5)$$

$$D = \sum_{k=1}^N \rho_k = 1, \quad (6)$$

where  $M$  is the total number of reflections with known phases,  $F_c(\mathbf{h}_j)$  is the calculated structure factor for reflection  $\mathbf{h}_j$ ,  $F_o(\mathbf{h}_j)$  is the observed structure factor, and  $\sigma_j$  is the estimated standard deviation (e.s.d.) of  $|F_o(\mathbf{h}_j)|$ . Equation (5) is referred to as the  $F$ -constraint ( $\chi^2$  statistics type), and Eq. (6) as the normalization constraint. When dealing with X-ray diffraction data of a compound where  $T$  is the total number of electrons in the unit cell,  $F_c(\mathbf{h}_j)$  is given as

$$F_c(\mathbf{h}_j) = T \sum_{k=1}^N \rho_k \exp(2\pi i \mathbf{h}_j \mathbf{r}_k). \quad (7)$$

Let  $\lambda$  and  $\mu$  be the Lagrange multipliers for  $C$  and  $D$ , respectively. Using the method of undetermined multipliers, we have

$$Q = S - \lambda(C - 1) - \mu(D - 1). \quad (8)$$

$Q$  can be maximized by setting the partial derivatives of  $Q$  with respect to  $\rho_k$ ,  $\lambda$ , and  $\mu$  at zero:

$$\frac{\partial Q}{\partial \rho_k} = 0, \quad (9)$$

$$\frac{\partial Q}{\partial \lambda} = 0, \quad (10)$$

$$\frac{\partial Q}{\partial \mu} = 0. \quad (11)$$

Then, the maximum-entropy (ME) equation is derived [19]:

$$\rho_k = \frac{\tau_k}{Z} \exp\left(-\lambda \cdot \frac{\partial C}{\partial \rho_k}\right) \quad (12)$$

with

$$Z = \sum_{k=1}^N \tau_k \exp\left(-\lambda \cdot \frac{\partial C}{\partial \rho_k}\right). \quad (13)$$

### 3.2 0th order and nonlinear single-pixel approximations

Equation (12) cannot be solved analytically. Then, Kumazawa *et al.* [19] introduced a 0th-order single-pixel approximation, where we expand the derivative of  $C$  with respect to  $\rho_k$  in a Taylor series

$$\frac{\partial C}{\partial \rho_k} = \frac{\partial C}{\partial \tau_k} + \sum_{l=1}^N (\rho_l - \tau_k) \cdot \frac{\partial^2 C}{\partial \tau_k \partial \tau_l} \quad (14)$$

and neglect the second term in the right side of Eq. (14). This linear approximation is equivalent to the simple replacement of  $\partial C / \partial \rho_k$  in Eq. (12) with  $\partial C / \partial \tau_k$ :

$$\rho_k = \frac{\tau_k}{Z} \exp\left(-\lambda \cdot \frac{\partial C}{\partial \tau_k}\right). \quad (15)$$

This equation means that the ME density distribution is reached through iterations  $n = 0, 1, 2, \dots$ :

$$\rho_k^{(n+1)} = \frac{\rho_k^{(n)}}{Z} \exp\left(-\lambda \cdot \frac{\partial C}{\partial \rho_k^{(n)}}\right). \quad (16)$$

We start MEM iterations, adopting the prior information

$$\rho_k^{(0)} = \frac{T}{V}, \quad (17)$$

*viz.*, a uniform density in the unit cell with the volume of  $V$ .

Because the second-order derivatives in the second term of Eq. (14) are independent of  $\rho$  and  $\lambda$ , the second term is regarded as proportional to only  $\Delta\rho = \rho_l - \tau_k$ . That is, the 0th-order single-pixel approximation as well as the iterative procedure represented as Eq. (16) is correct provided that  $\Delta\rho = \rho_k^{(n+1)} - \rho_k^{(n)}$  is negligibly small. The only way to solve this problem is to choose a sufficiently small  $\lambda$  value, which leads

to an increase in the total number of iterations. However, the 0th-order single-pixel approximation works well in nearly every case.

In an alternative method to solve Eq. (12), we use part of the second term in Eq. (14), *i.e.*, only the term for  $k = l$  in the summation, which is referred to as nonlinear single-pixel approximation [20].  $Q$  is optimized by the Newton-Raphson method:

$$Q(\rho + \Delta\rho) = Q(\rho) + \Delta\rho \cdot \frac{\partial Q}{\partial \rho} + \frac{(\Delta\rho)^2}{2} \cdot \frac{\partial^2 Q}{\partial \rho^2}. \quad (18)$$

The partial derivative of  $Q(\rho + \Delta\rho)$  with respect to  $\rho$  is zero provided that

$$\Delta\rho = -\left(\frac{\partial^2 Q}{\partial \rho^2}\right)^{-1} \cdot \frac{\partial Q}{\partial \rho} \quad (19)$$

and

$$\rho^{(n+1)} = \rho^{(n)} + \Delta\rho. \quad (20)$$

The Newton-Raphson method permits prompt convergence to the solution, decreasing the total number of iterations considerably.

### 3.3 How to deal with elements of negative coherent-scattering lengths

MEM is simply applicable to the analysis of  $F_o$  data for compounds containing elements with negative  $b_c$  values [21–23]. In such cases,  $S$  is represented as the sum of those for positive and negative densities:

$$S = S^+ + S^-. \quad (21)$$

This is a good approximation to  $S$  because of the negligible overlap of nuclear densities for two atoms. Thus, Eq. (7) is rewritten as

$$F_c(\mathbf{h}_j) = \sum_{k=1}^N (\rho_k^+ + \rho_k^-) \exp(2\pi i \mathbf{h}_j \mathbf{r}_k) \quad (22)$$

with

$$\rho_k^+ = T^+ \rho_k, \quad (23)$$

$$\rho_k^- = T^- \rho_k; \quad (24)$$

$T^+$  and  $T^-$  are the total numbers of positive and negative  $b_c$ 's, respectively;  $\rho_k$  is the nuclear density normalized with Eq. (6). We can reach the ME nuclear-density distribution by solving the following equation iteratively:

$$\rho_k^\pm = \frac{\tau_k^\pm}{Z^\pm} \exp\left(-\lambda \cdot \frac{\partial C}{\partial \rho_k^\pm}\right). \quad (25)$$

### 3.4 Calculations of structure factors

Let  $P$  be the number of symmetry operations, and  $R_l$  the symmetry-operation matrix, then the real part,  $F_c(\text{real})$ , and the imaginary part,  $F_c(\text{imag.})$ , of  $F_c(\mathbf{h}_j)$  in Eq. (7) for X-ray diffraction are computed from [13]

$$F_c(\text{real}) = T \sum_{k=1}^N \rho_k W_{jk}(\text{real}), \quad (26)$$

$$F_c(\text{imag.}) = T \sum_{k=1}^N \rho_k W_{jk}(\text{imag.}), \quad (27)$$

where

$$W_{jk}(\text{real}) = \sum_{l=1}^P \cos(2\pi \mathbf{h}_j R_l \mathbf{r}_k), \quad (28)$$

$$W_{jk}(\text{imag.}) = \sum_{l=1}^P \sin(2\pi \mathbf{h}_j R_l \mathbf{r}_k). \quad (29)$$

$F_c(\text{imag.})$  is necessary only in noncentrosymmetric space groups.

In PRIMA,  $W_{jk}(\text{real})$  and  $W_{jk}(\text{imag.})$  associated with phases are first calculated for the asymmetric unit and stored in two-dimensional arrays allocated dynamically. The continuous use of storage for the arrays allocated dynamically accelerates the execution speed of PRIMA dramatically.

In a relatively large system containing many reflections and pixels in the asymmetric unit, the calculations of  $W_{jk}(\text{real})$  and  $W_{jk}(\text{imag.})$  are rate-determining steps in MEM analysis. We restructured this part fundamentally, fully utilizing space-group symmetry, diffraction properties, and fast evaluation of sine and cosine functions without sacrificing accuracy virtually, which considerably accelerates the calculations of the two arrays. Details in this revolutionary breakthrough in MEM analysis will be reported elsewhere [12].

### 3.5 Initial value of $\lambda$ and its adjustment

Learned information is needed to set the initial value of  $\lambda$ ,  $\lambda_0$ , appropriately. With too small  $\lambda_0$ , the convergence will be slow and may not reach  $C = 1$ . On the other hand, the convergence will never be attained when  $\lambda_0$  is too large. PRIMA has a feature of automatic estimation of  $\lambda_0$  by using one of the following three equations:

$$\lambda_0 = G \ln 10, \quad (30)$$

$$\lambda_0 = A_0 + \frac{A_1}{(G - A_2)^2 - A_3}, \quad (31)$$

$$\lambda_0 = B_0 + B_1 G + B_2 G^2, \quad (32)$$

where

$$G = \left( \frac{1}{M} \sum_{j=1}^M \frac{1}{\sigma_j^2} \right)^{-1}, \quad (33)$$

and  $A_0, A_1, A_2, A_3, B_0, B_1$ , and  $B_2$  are constants determined empirically. With Eqs. (30)–(32), PRIMA is mostly capable of estimating appropriate  $\lambda_0$ .

PRIMA has another feature of adjusting  $\lambda$  automatically during MEM iterations. In this technique,  $\lambda$  in the  $(n+1)$ 'th iteration ( $n = 1, 2, \dots$ ),  $\lambda^{(n+1)}$ , is automatically adjusted with a coefficient,  $t$ :

$$\lambda^{(n+1)} = \lambda^{(n)} + t\lambda_0 \quad (34)$$

with

$$\lambda^{(1)} = \lambda_0. \quad (35)$$

If  $t = 0$  (no adjustment, default value),  $\lambda$  is not varied. When the MEM iterations tend toward divergence,  $\lambda^{(n+1)}$  is decreased to  $\lambda^{(n)}/2$ . Four different options are implemented in PRIMA for the adjustment of  $\lambda$ :

1.  $\lambda_0$  is input from a file, and  $\lambda$  remains constant.
2.  $\lambda_0$  is input from a file, and  $\lambda$  is adjusted.
3.  $\lambda_0$  is automatically determined, and  $\lambda$  remains constant.
4.  $\lambda_0$  is automatically determined, and  $\lambda$  is adjusted.

For example, we have empirically learned that the second option is the best selection in the nonlinear approximation method. This finding is explained in terms of the fact that, in the nonlinear single-pixel approximation introducing the Newton-Raphson method,  $\lambda_0$  must be very small, which may lead to a failure in the automatic adjustment of  $\lambda$ .

### 3.6 $R$ factors

Two  $R$  factors, which are measures of reliability of MEM analysis, are defined as

$$R_F = \frac{\sum_{j=1}^M |F_c(\mathbf{h}_j) - F_o(\mathbf{h}_j)|}{\sum_{j=1}^M |F_o(\mathbf{h}_j)|} \quad (36)$$

and

$$R_{wF} = \left[ \frac{\sum_{j=1}^M \sigma_j^{-2} |F_c(\mathbf{h}_j) - F_o(\mathbf{h}_j)|^2}{\sum_{j=1}^M \sigma_j^{-2} |F_o(\mathbf{h}_j)|^2} \right]^{1/2}. \quad (37)$$

### 3.7 Appropriate pixel numbers

Under favor of space-group symmetry [24], densities in the asymmetric unit are calculated with Eq. (16).  $N_a$ ,  $N_b$ , and  $N_c$  have to be set so as to satisfy the space-group symmetry. For example, fractional coordinates ( $x$ ,  $y$ , and  $z$ ) in the asymmetric unit for space group  $Fm\bar{3}m$  (No. 225) has the following ranges [24]:

$$0 \leq x \leq \frac{1}{2}, \quad (38)$$

$$0 \leq y \leq \frac{1}{4}, \quad (39)$$

$$0 \leq z \leq \frac{1}{4}. \quad (40)$$

Then,  $N_a$  must be even while  $N_b$  and  $N_c$  must be multiples of 4; for example,  $N_a = 82$ ,  $N_b = 128$ , and  $N_c = 128$ . Fractional coordinates in the asymmetric unit for space group  $Pm$  (No. 6, unique axis  $b$ ) [24] are confined to

$$0 \leq x \leq 1, \quad (41)$$

$$0 \leq y \leq \frac{1}{2}, \quad (42)$$

$$0 \leq z \leq 1. \quad (43)$$

In this case,  $N_b$  should be even whereas  $N_a$  and  $N_c$  may be any integers large enough for MEM analysis. It is further preferable that symmetry elements such as rotation axes and inversion centers are located on intersections of grid lines. For further guidelines concerning the setting of pixel numbers, refer to Refs. [25, 26].

## 4. DERIVATION OF INTEGRATED INTENSITIES FROM POWDER DIFFRACTION DATA

In the MEM analysis of relatively simple structures from powder diffraction data,  $|F_{ok}|$  is usually obtained by pattern decomposition such as individual profile fitting [27], the Pawley method [28], and the Le Bail method [29]. However, most values of  $|F_{ok}|$  for

compounds exhibiting heavily overlapped reflections can hardly be estimated by pattern decomposition without introducing any structural models.

After Rietveld analysis, the ‘observed’ integrated intensity,  $I_{ok}$ , for reflection  $k$  is approximately computed by apportioning the net diffraction intensity,  $y_i - y_b(2\theta_i)$ , at step  $i$  in the ratio of contributions of overlapping reflections ( $K = 1, 2, 3, \dots$ ) [5]:

$$I_{ok} = \sum_i [y_i - y_b(2\theta_i)] \frac{Y_{ik}}{\sum_K Y_{iK}}, \quad (44)$$

where  $y_i$  is the observed intensity;  $y_b(2\theta_i)$  is the background function;  $Y_{ik}$  and  $Y_{iK}$  are the contributions of reflections  $k$  and  $K$  to the net diffraction intensity at step  $i$ , respectively. The summations  $\sum_i$  and  $\sum_K$  are carried out over all the data points contributing to the profile of reflection  $k$  and over all the reflections contributing to  $y_i - y_b(2\theta_i)$ , respectively. In the cases of isolated reflections, Eq. (44) reduces to

$$I_{ok} = \sum_i [y_i - y_b(2\theta_i)]. \quad (45)$$

Consequently, fairly accurate  $I_{ok}$  is obtainable in a model-free fashion as long as the background can be adequately approximated by  $y_b(2\theta_i)$ . Equations (44) and (45) are also used to derive  $I_{ok}$  after each cycle in Le Bail refinement [29].

$Y_{ik}$  is evaluated from scale factor  $s$ , multiplicity  $m_k$ , preferred-orientation factor  $P_k$ , Lorentz-polarization factor  $L_k$ , structure factor calculated from structure parameters  $F_{ck}$ , and profile function  $f(2\theta_i - 2\theta_k)$ :

$$Y_{ik} = sm_k P_k L_k |F_{ck}|^2 f(2\theta_i - 2\theta_k). \quad (46)$$

Substituting  $K$  for  $k$  in this equation yields  $Y_{iK}$ .  $F_{ck}$  is calculated from structure parameters (fractional coordinates, occupancies, and isotropic/anisotropic atomic displacement parameters) refined in Rietveld analysis. The observed scattering amplitude,  $|F_{ok}|$ , is estimated with

$$|F_{ok}| = \left( \frac{I_{ok}}{sm_k P_k L_k} \right)^{1/2}. \quad (47)$$

Takata *et al.* [3, 4] applied the above procedure (MEM/Rietveld method) to the estimation of  $|F_{ok}|$ 's analyzed by MEM. However, electron densities derived from the  $|F_{ok}|$ 's are subject to the structural

model in Rietveld analysis because Eq. (46) contains  $F_{ok}$ . This undesirable effect enlarges with increasing degree of overlap of reflections, lowering the accuracy of final densities necessarily. MEM can extract structural details from the  $|F_{ok}|$  data estimated in the above way because they involve contributions neglected in the structural model. Furthermore,  $|F_{ok}|$  for an isolated reflection can simply be determined without any structural model, as described earlier. Visualization of diffraction data by the combination of Rietveld and MEM analyses, therefore, serves the modification of imperfect structural models [30–33]. Nevertheless, the dependence of electron-density distribution on the structural model casts a gloom over the combined use of the Rietveld and maximum-entropy methods.

## 5. PROCEDURE OF MEM-BASED PATTERN FITTING

To minimize the bias imposed on electron densities by the structural model, we devised the following iterative procedure of MPF [8, 9]:

1. Intensity data are analyzed by the Rietveld method.
2.  $|F_{ok}|$ 's are approximately evaluated with Eqs. (44)–(47).
3. The  $|F_{ok}|$ 's with phases,  $\psi$ , derived from the Rietveld analysis, are analyzed by MEM to yield 3D electron densities,  $\rho(x, y, z)$ . Then,  $F_{Mk}$  is computed by the Fourier transform of  $\rho(x, y, z)$  in the unit cell:

$$F_{Mk} = V \iiint \rho(x, y, z) \exp[2\pi i(hx + ky + lz)] dx dy dz. \quad (48)$$

4. The resulting  $\rho(x, y, z)$  data are visualized in three dimensions.
5. After close examination of the electron-density image, return to step 1 to modify the structural model if necessary.
6. The model function is fit to the whole observed diffraction pattern by refining parameters irrelevant to the crystal structure: scale factor, pro-

file parameters, peak-shift parameters, and background parameters. Each structure factor in the model function is not calculated from any structure parameters but fixed at  $F_{Mk}$ .

7. Terminate unless decreases in  $R$  factors in step 6 are significant compared with those in the previous whole-pattern fitting.
8. Return to step 2.

Steps 2–8 repeated till the convergence is attained is referred to as REMEDY cycles, serving to minimize the bias imposed by the structural model in Rietveld analysis. The influence of the structural model in the Rietveld analysis on  $\rho(x, y, z)$ 's diminishes by repeating REMEDY cycles. In other words, intensity partitioning for overlapping reflections becomes more accurate with increasing number of iterations owing to derivation of additional structural information by MEM. Such an iterative method is somewhat similar to the Le Bail method [29] but differs from it in the point that structure factors in whole-pattern fitting are fixed at values of  $F_{Mk}$  resulting from the previous MEM analysis.

**Figure 1** illustrates the above sequence schematically. ‘Rietveld’, ‘MEM’, and ‘w.p.f.’, each in a pair of parentheses, denote analyses whereby structure factors are derived.  $F_o(\text{Rietveld})$  and  $F_o(\text{w.p.f.})$  in this figure correspond to  $F_{ok}$ , and  $F_c(\text{MEM})$  is equivalent to  $F_{Mk}$ . Contributions of anomalous dispersion to structure factors must be excluded in MEM analysis in the same way as in Fourier synthesis whereas they should be included in whole-pattern fitting. In other words, structure parameters are used only to add anomalous dispersion corrections to structure factors in MPF.

Structural details are changed in step 3 while the goodness-of-fit is improved by fixing each structure factor at  $F_{Mk}$  in step 6. The effect of the structural model in the Rietveld analysis on  $F_{Mk}$  diminishes with increasing number of REMEDY cycles. We can therefore approach the final structure reflecting the observed intensity data more closely. Step 6 is not Rietveld analysis but MPF to obtain values of  $F_{ok}$  containing additional information about structural details.

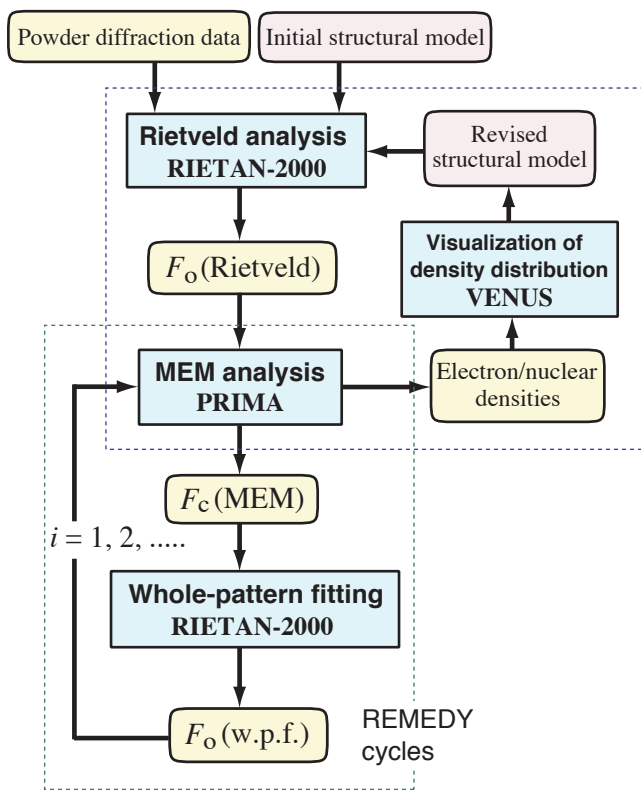


Fig. 1 Structure refinement by MEM/Rietveld analyses followed by iterative MEM-based pattern fitting.

Takata et al. [3, 4] have been utilizing not all the processes shown in Fig. 1 but only the part of iterative MEM/Rietveld analyses (inside the upper box consisting of broken lines) for modifying structural models. As described in Sect. 4, the MEM/Rietveld method is a tepid approach to the determination of electron/nuclear densities because no structural information extracted by MEM from powder diffraction data is reused by executing w.p.f. after the MEM analysis. The MEM/Rietveld method should be used only to modify structural models imperfect with respect to sites (defects) unfindable and overlooked in the models.

MPF is capable of modeling disordered atomic configurations [32, 34], chemical bonds, nonlocalized electrons, and anharmonic thermal motion [36] more adequately than the conventional Rietveld method. These purposes are attainable more satisfactorily by MPF than with programs for conventional Rietveld analysis because crystal structures are represented not by structure parameters (fractional coordinates, occupancies, and atomic displacement parameters)

but also by 3D electron/nuclear densities. The establishment of MPF leads to the availability of an ultra-high-resolution ‘X-ray/neutron microscope’ that allows us to visualize powder diffraction data as 3D density images. X-Ray and neutron diffraction should be utilized complementarily for (a) the more adequate expression of chemical bonds and (b) the analysis of anharmonic thermal vibration and disordered structures, respectively.

## 6. SOFTWARE FOR MPF

We have developed a state-of-the-art system for structure refinement by MPF. This free software comprises a multi-purpose pattern fitting program, RIETAN-2000, for angle-dispersive X-ray and neutron diffraction [9, 11], MEM analysis program and PRIMA [12], and VENUS [14] for 3D visualization of crystal structures and electron/nuclear densities.<sup>1</sup>

The goodness-of-fit must reach a high level to minimize the influence of the structural model on densities resulting from MPF. We have been utilizing our original technique of partial profile relaxation [11] in both Rietveld analysis and whole-pattern fitting. At present, MPF would not function well without this feature, which was certainly effective in MPF structure refinements described later.

MEED [13] is now obsolete; our original program, PRIMA, can carry out MEM analyses incomparably faster than MEED thanks to the full optimization of its code, as described in Sect. 3. RIETAN-2000 provides PRIMA with structural information, and *vice versa*, through two files storing  $F_{ok}$  data (\*.mem) and  $F_{Mk}$  data (\*.fba).

VENUS bears the bell in 3D visualization, rendering, and manipulation of crystal structures and electron/nuclear densities determined not only by X-ray/neutron diffraction but by electronic-structure calculations using Gaussian 98 [37], SCAT [38], and WIEN2k [39]. VENUS fully utilizes the OpenGL Application Programming Interface (API) with the graphical user interface constructed with GLUT and GLUI. Video cards equipped with GPU’s supporting hardware acceleration for the OpenGL are desired to

<sup>1</sup>RIETAN-2000, PRIMA, and VENUS can be downloaded from <http://homepage.mac.com/fujioizumi/index.html>.

rotate, expand, and translate objects fast in three dimensions.

The VENUS system consists of two independent programs: VICS (**VI**sualization of **C**rystal **S**tructures) and VEND (**V**isualization of **E**lectron/**N**uclear **D**ensities). That is, VEND and VICS deal with electron/nuclear densities and crystal structures, respectively VEND also supports the 3D visualization of electrostatic potentials and wave functions that have both positive and negative values, which allows us to obtain additional information about electronic states.

## 7. DATA USED IN MPF AND ITS KNOW-HOW

### 7.1 Three reflection types

The algorithm for the MEM analysis of  $F_{ok}$ 's is, *per se*, the same regardless of diffraction procedures. Some special techniques are, however, required to analyze  $F_{ok}$ 's derived from powder data. The MEM deals with  $|F_{ok}|$ 's of reflections whose phases have been estimated by some means. A reflection whose  $|F_{ok}|$  is computed from Eqs. (44)–(47) at the end of Rietveld analysis is referred to as a type 1 reflection.  $F_{ok}$ 's of overlapped reflections evaluated according to Rietveld's procedure [5] are influenced by the refined structure in a varying degree. The sum of  $|F_{ok}|$ 's is then assigned to a group of overlapped reflections belonging to type 2 to enhance the ability of estimation by MEM. In the case of type 3 reflections, their peak positions are so near to  $2\theta_{\max}$  that parts of their profiles extend beyond  $2\theta_{\max}$ . Nevertheless, we should also calculate the  $F_{Mk}$  of a type 3 reflection because excluding them necessarily brings about a bad profile fit near  $2\theta_{\max}$ .  $F_{Mk}$  for the type 3 reflection is thus estimated from electron densities determined from only  $F_{ok}$  for reflections of types 1 and 2. Type 2 reflections are decomposed to afford their individual  $F_{ok}$ 's.  $F_{ok}$ 's, sums of  $F_{ok}$ 's, and only  $hkl$  indices are output for reflections with types 1, 2, and 3, respectively.

### 7.2 Structural data input/output during MPF

Prior to MEM analysis, we need to estimate  $F_{ok}$ 's and the e.s.d.'s of  $|F_{ok}|$ 's:  $\sigma(|F_{ok}|)$  at any rate. It should be

emphasized that *the  $F_{ok}$  and  $\sigma(|F_{ok}|)$  data of all the low- $Q$  (large- $d$ ) reflections are indispensable to MEM analysis.* The lack of these data is fatal, necessarily leading to a failure in the MEM analysis.

Let  $\sigma(I_{ok})$  and  $\sigma(s)$  be the e.s.d.'s of  $I_{ok}$  and  $s$ , respectively, then the estimated standard deviation (e.s.d.),  $\sigma(|F_{ok}|)$ , of  $|F_{ok}|$  for a type 1 reflection is estimated from

$$\sigma(|F_{ok}|) = \frac{|F_{ok}|}{2} \left\{ \left[ \frac{\sigma(I_{ok})}{I_{ok}} \right]^2 + \left[ \frac{\sigma(s)}{s} \right]^2 \right\}^{1/2}. \quad (49)$$

Note that  $\sigma(|F_{ok}|)$  is *not actually observed but calculated* from  $|F_{ok}|$  and  $I_{ok}$ , suffering from errors due to the bias toward a structural model in Rietveld analysis in the same manner as with  $|F_{ok}|$ . Further, Eq. (49) is based on only counting statistics, neglecting the overlap of reflections. We must, hence, keep in mind that  $\sigma(|F_{ok}|)$  values estimated from powder diffraction data are not very accurate.

The sum of  $|F_{ok}|$ 's,  $G_o$ , for a group of type 2 reflections is given by

$$G_o = \left( \frac{\sum_k I_{ok}}{s \sum_k m_k P_k L_k} \right)^{1/2} \quad (50)$$

with the summation  $\sum_k$  carried out over all the overlapped reflections. The e.s.d. of  $G_o$  is estimated by

$$\sigma(G_o) = \frac{G_o}{2} \left\{ \left[ \frac{\sigma(\sum_k I_{ok})}{\sum_k I_{ok}} \right]^2 + \left[ \frac{\sigma(s)}{s} \right]^2 \right\}^{1/2} \quad (51)$$

analogous to Eq. (49).

At the end of the whole-pattern fitting,  $I_{ok}$  is evaluated in a similar manner to Eq. (44):

$$I_{ok} = \sum_i \left[ y_i - y_b(2\theta_i) \right] \frac{Y'_{ik}}{\sum_K Y'_{iK}}. \quad (52)$$

$Y'_{ik}$  is the contribution of reflection  $k$  to the net diffraction intensity and given by

$$Y'_{ik} = sm_k P_k L_k |F_{Mk}|^2 f(2\theta_i - 2\theta_k). \quad (53)$$

In this equation,  $F_{ck}$  in Eq. (46) is replaced with  $F_{Mk}$ . On substitution of  $K$  for  $k$  in this equation, we obtain  $Y'_{ik}$ .  $|F_{ok}|$  and  $\sigma(I_{ok})$  are respectively computed with Eqs. (47) and (14) in the same manner as their calculations after the Rietveld analysis [1]. Because

overlapped reflections are decomposed during the first MEM analysis without any structural model, they are regarded as type 1 reflections in subsequent processes.

When analyzing neutron diffraction data or X-ray diffraction data for centrosymmetric structures,  $|F_{ok}|$  for a profile-relaxed reflection can directly be refined in whole-pattern fitting with RIETAN-2000. This unique feature is expected to accelerate the convergence of structure refinement, provided that calculated profiles are in good agreement with observed ones for the relaxed reflections.

### 7.3 Distribution of $\epsilon(\text{Gauss})$

The use of the  $\chi^2$  statistics in the constraint function (5) is based on the assumption that the experimental errors,  $\sigma(|F_{ok}|)$ , are random with a Gaussian distribution:

$$\epsilon(\text{Gauss}) = \frac{|F_{Mk}| - |F_{ok}|}{\sigma(|F_{ok}|)}, \quad (54)$$

where  $\epsilon(\text{Gauss})$  is a sample of the random variable with normalized Gaussian distribution [40]. No satisfactory result can be obtained when the distribution of  $\epsilon(\text{Gauss})$ 's is far from Gaussian. PRIMA has a feature to output a text file storing  $\epsilon(\text{Gauss})$  values with either of two formats: a raw data file, \*.raw, and an Igor text file, \*.err. We can easily examine the distribution of  $\epsilon(\text{Gauss})$  using this file.

### 7.4 Strategy for stable convergence

We should pay attention to electron-density maps obtained from  $F_{Mk}$  data in addition to the convergence test in each iteration. There is particularly a fair chance for structural estimation to be misdirected at the first iteration. Accordingly, we need to repeat steps 2–8 while comparing density maps resulting from MEM analysis with those obtained from  $F_{ck}$ 's. This comparison is needed to judge whether the electron-density distribution is affected by the structural model or estimated properly by MEM. For reflections with unsatisfactory fits between observed and calculated intensities, e.s.d.'s obtained with Eqs. (49) and (51) should appropriately be increased to enhance the degree of freedom in estimation by MEM; such large residuals usually arise from imperfect representation of the real structure on condition that the

intensity data are collected appropriately. If this part were partitioned among overlapped reflections in proportion to their values of  $Y_{iK}$ , MEM would estimate the structure in a way biased in favor of the structural model.

The efficiency of REMEDY cycles depends on the validity of the starting structural model. If the structure refined in step 1 differs considerably from the real one, MEM analysis may fail in structure refinement owing to the inaccurate partition of observed Bragg intensities among overlapped reflections.

$R$  factors in the whole-pattern fitting are used as the measure of the convergence in REMEDY cycles.  $R$  factors in model-free MEM analysis are comparable regardless of the progress of the REMEDY cycles because the convergence criterion is a constraint function being equal to unity. Accordingly,  $R$  factors for MEM, Eqs. (36) and (37), should not be used to judge the convergence of the iterations.

## 8. EXAMPLES OF APPLYING MPF TO VARIOUS MATERIALS

### 8.1 Positional disorder of $\text{K}^+$ ions interlayered in $\text{K}_x\text{Ti}_{2-x/3}\text{Li}_{x/3}\text{O}_4$

A layered compound,  $\text{K}_x\text{Ti}_{2-x/3}\text{Li}_{x/3}\text{O}_4$  (space group:  $Cmcm$ ) contains (a) lepidocrocite-like  $\text{Ti}_{2-x/3}\text{Li}_{x/3}\text{O}_4$  layers consisting of edge-sharing (Ti,Li) $\text{O}_6$  octahedra and (b) charge-balancing  $\text{K}^+$  ions in the interlayer domain [41]. Rietveld analysis from neutron diffraction data showed  $\text{K}^+$  ions to be highly disordered between two layers. With a split-atom model, the positional disorder of  $\text{K}^+$  ions could not adequately be expressed in view of an extraordinarily large isotropic atomic displacement parameter,  $B$ , of ca.  $10 \text{ \AA}^2$  for K.

We determined electron densities in  $\text{K}_x\text{Ti}_{2-x/3}\text{Li}_{x/3}\text{O}_4$  ( $x = 0.8$ ) to visualize how  $\text{K}^+$  ions are distributed in between  $\text{Ti}_{2-x/3}\text{Li}_{x/3}\text{O}_4$  layers [42]. Its X-ray powder diffraction data were measured at room temperature with Cu  $K\alpha$  radiation on a MAC Science MXP 3TZ diffractometer with a vertical  $\theta:\theta$  configuration and a pair of long Soller slits with an aperture angle of  $1^\circ$ . The same diffractometer was used in X-ray powder diffraction experiments that will be described in 8.1–8.3.

The diffraction data were analyzed by the Rietveld

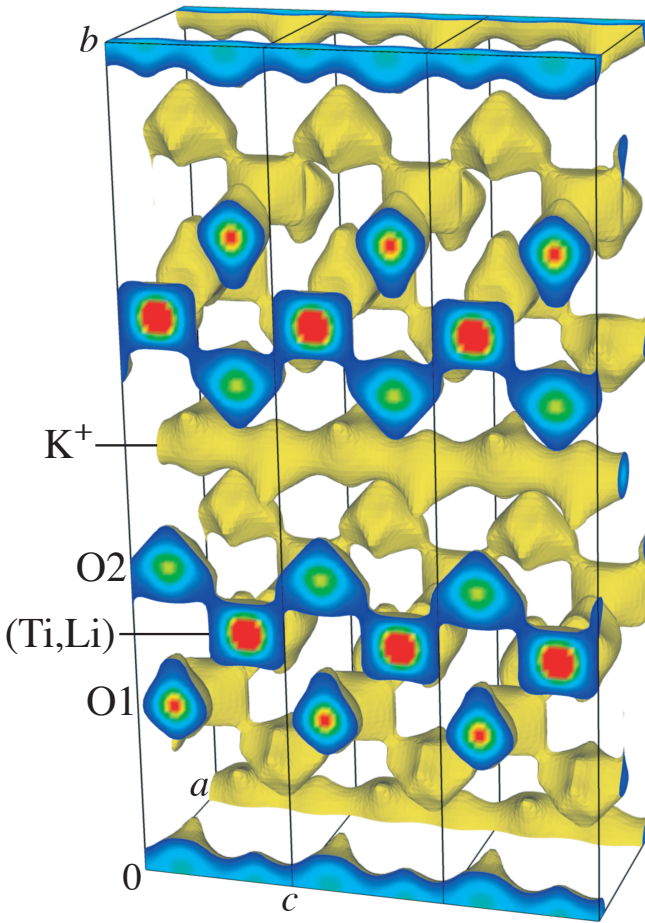


Fig. 2 Electron-density distribution determined by MPF for  $K_x\text{Ti}_{2-x/3}\text{Li}_{x/3}\text{O}_4$  ( $x = 0.8$ ). Isosurfaces in three unit cells were drawn for an equidensity level of  $1.2/\text{\AA}^3$ .

method on the basis of space group  $Cmcm$  [41]. We assumed the random occupation of the same octahedral site ( $4c$ ) by  $\text{Ti}^{4+}$  and  $\text{Li}^+$  ions. Final  $R$  factors [43] were  $R_{\text{wp}} = 11.51\%$  ( $S = R_{\text{wp}}/R_e = 1.08$ ) and  $R_B = 5.75\%$ . Subsequent three REMEDY cycles lowered  $R_{\text{wp}}$  to  $10.59\%$  ( $S = 1.00$ ) and  $R_B$  to  $1.91\%$ . The dramatic decrease in  $R_B$  is ascribable to the better representation of the structural details by calculating structure factors from electron densities than from structure parameters in Rietveld analysis.

**Figure 2** shows isosurfaces of electron densities (number densities of electrons) in  $K_x\text{Ti}_{2-x/3}\text{Li}_{x/3}\text{O}_4$  ( $x = 0.8$ ). Neither negative densities nor distinct ripples appeared at all, which is a great advantage of MEM over Fourier synthesis. A winding stream of  $\text{K}^+$  ions along the  $[001]$  direction and  $(\text{Ti,Li})\text{-O}$  bonds were clearly visualized by virtue of MPF. The positional disorder of  $\text{K}^+$  ions is partly ascribable to large

differences in the oxidation states and effective ionic radii,  $r$ , between  $\text{Ti}^{4+}$  ( $r = 0.605 \text{\AA}$ ) and  $\text{Li}^+$  ( $r = 0.76 \text{\AA}$ ) ions sharing the same octahedral site. Thus, our first challenge to the determination of spatial distribution for highly disordered species was quite successful.

MPF is expected to be effective for intercalation and clathrate compounds where guests have often disordered configurations. In these compounds, split-atom models may fail in providing reasonable atomic displacement parameters or sufficiently low  $R$  factors. We will further apply MPF to such systems extensively.

## 8.2 Atomic arrangement of K clusters in a K-doped zeolite K-LTA

The synthetic zeolite, Linde Type A (LTA), consists of  $\alpha$ - and  $\beta$ -cages arrayed alternately like atoms in the CsCl-type compound with inner diameters of  $11 \text{\AA}$  and  $7 \text{\AA}$ , respectively. Alkali metal ions are usually incorporated into the cages to neutralize negative charges of the LTA framework. K-type LTA (K-LTA) doped with excess K ( $K_x\text{@K-LTA}$ ) is of interest in connection with its ferromagnetism in the absence of magnetic atoms below  $7 \text{ K}$  [44]. Because the excess K atoms release  $4s$  electrons to change into  $\text{K}^+$  ions,  $K_x\text{@K-LTA}$  is regarded as a strongly-correlated electron system. To understand the mechanism of the anomalous magnetic property, nuclear and electron densities in  $K_x\text{@K-LTA}$  were determined by MPF from neutron and X-ray diffraction data, respectively [9, 45]. The neutron diffraction data of  $K_{5.8}\text{@K-LTA}$  were measured at  $40 \text{ K}$  on HRPD at JRR-3M (JAERI) with  $\lambda = 1.824 \text{\AA}$ , and the X-ray diffraction data of  $K_{5.2}\text{@K-LTA}$  at room temperature.

Rietveld refinements revealed that space group  $Fm\bar{3}c$  in K-LTA changes to  $F23$  with lower symmetry in  $K_x\text{@K-LTA}$  [46]. However, the disorder of K atoms cannot sufficiently be represented in these structure refinements. After one cycle of MEM-based whole-pattern fitting with the neutron diffraction data,  $R_{\text{wp}}$  slightly decreased from  $5.03\%$  ( $S = 1.48$ ) to  $4.92\%$  ( $S = 1.45$ ), and  $R_B$  from  $2.05\%$  to  $1.91\%$ , respectively. *i.e.*, from  $8.25\%$  ( $S = 1.08$ ) to  $7.30\%$  ( $S = 0.96$ ) for  $R_{\text{wp}}$ . On the other hand, the goodness-

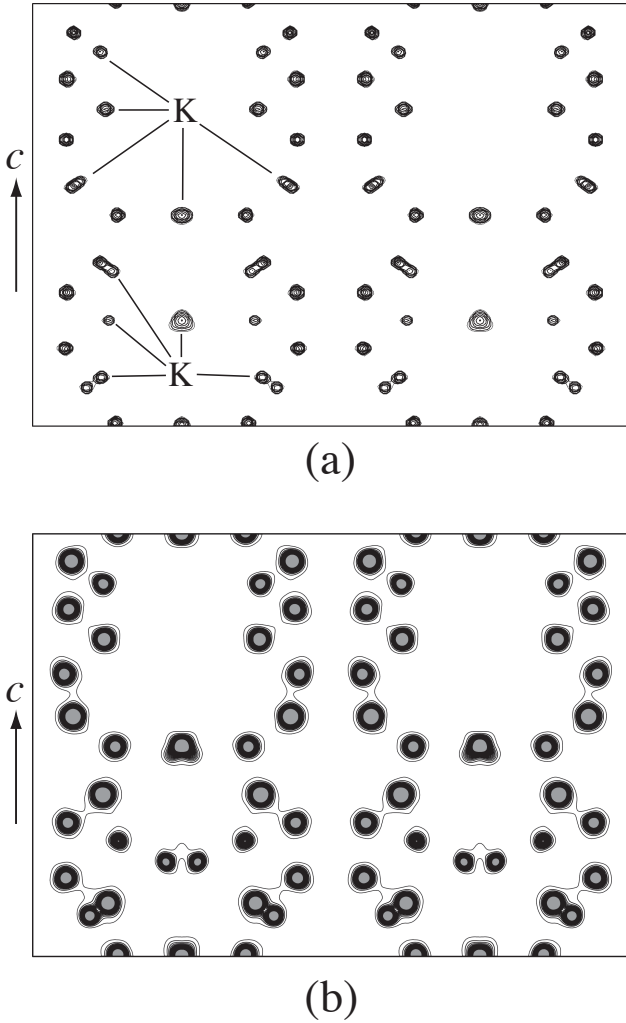


Fig. 3 (a) Nuclear- and (b) electron-density distribution on the (110) plane in  $K_{5.8}@K\text{-LTA}$  and  $K_{5.2}@K\text{-LTA}$ , respectively. Contours were plotted for (a)  $0.3 \times 2.1^n \text{ fm}/\text{\AA}^3$  ( $n = 1-9$ ) and (b)  $0.3-10/\text{\AA}^3$  with a step of  $0.4/\text{\AA}^3$ .

of-fit was improved more significantly with X-ray diffraction data, and from 2.70 % to 1.30 % for  $R_B$  after two REMEDY cycles. Such differences are believed to reflect (a) much wider spatial distribution of electrons in comparison with atomic nuclei and (b) the highly covalent nature of Si–O and Al–O bonds in the framework.

Nuclear and electron densities on the (110) plane are plotted in **Fig. 3**, where each quarter corresponds to an  $\alpha$ -cage.  $K^+$  ions are situated in the neighborhood of 4, 6, and 8-membered rings. Additional  $K^+$  ions are mainly included in the four- and eight-membered rings of the framework and partially oc-

cupy the center of an  $\alpha$  cage.  $K^+$  ions near the center of the six-membered ring form two kinds of tetrahedral assemblies occupied statistically. Adjacent  $\alpha$ -cages contain nonequivalent K clusters with different magnetic moments. The difference in the number of K atoms between the two types of the  $\alpha$ -cages was *ca.* 2 in a sample with the highest degree of spontaneous magnetization, which will give rise to the ferromagnetism with antiferromagnetic components. Adjacent  $\alpha$ -cages contain nonequivalent K clusters with different magnetic moments. The difference in the number of K atoms between the two types of the  $\alpha$ -cages was *ca.* 2 in a sample with the highest degree of spontaneous magnetization, which will give rise to the ferromagnetism with antiferromagnetic components.

### 8.3 Nuclear/electron-density distribution in the superconductor $\text{HgBa}_2\text{CuO}_{4+\delta}$

We prepared a high- $T_c$  superconductor  $\text{HgBa}_2\text{CuO}_{4+\delta}$  ( $T_c = 97 \text{ K}$ ; space group  $P4/mmm$ ) where the content of  $\text{CO}_3^{2-}$  ions substituting for  $[\text{O}_2\text{-Hg-O}_2]^{2-}$  ions was minimized to distribute excess oxygen atoms very uniformly by  $\text{O}_2$  annealing for a long time [47]. Its neutron and X-ray diffraction data were collected at room temperature on HRPD ( $\lambda = 1.823 \text{ \AA}$ ) and the MXP 3TZ diffractometer, respectively.

In structure refinements from both the neutron and X-ray powder diffraction data, MPF afforded lower  $R$  factors than conventional Rietveld analysis [9, 48]. The decrease in  $R_B$  achieved in the MPF analysis of the X-ray diffraction data was particularly pronounced, *i.e.*, from 1.66 % in the final Rietveld analysis to 0.89 % after two REMEDY cycles. No bonding electrons are explicitly taken into account in the Rietveld method whereby structure parameters are refined. On the other hand, MEM analysis enables us to express chemical bonds with electron densities in a higher degree of freedom, which is responsible for the close approach of  $F_c(\text{MEM})$  towards  $F_o(\text{w.p.f.})$ . In fact, densities of bonding electrons between metal and oxygen atoms varied appreciably during the REMEDY cycles. **Figure 4** shows substantial changes in electron densities corresponding to Cu–O1 bonds on the  $\text{CuO}_2$  conduction sheet in three refinement stages. This fact offers unambiguous evidence for introduction of additional structural information extracted by

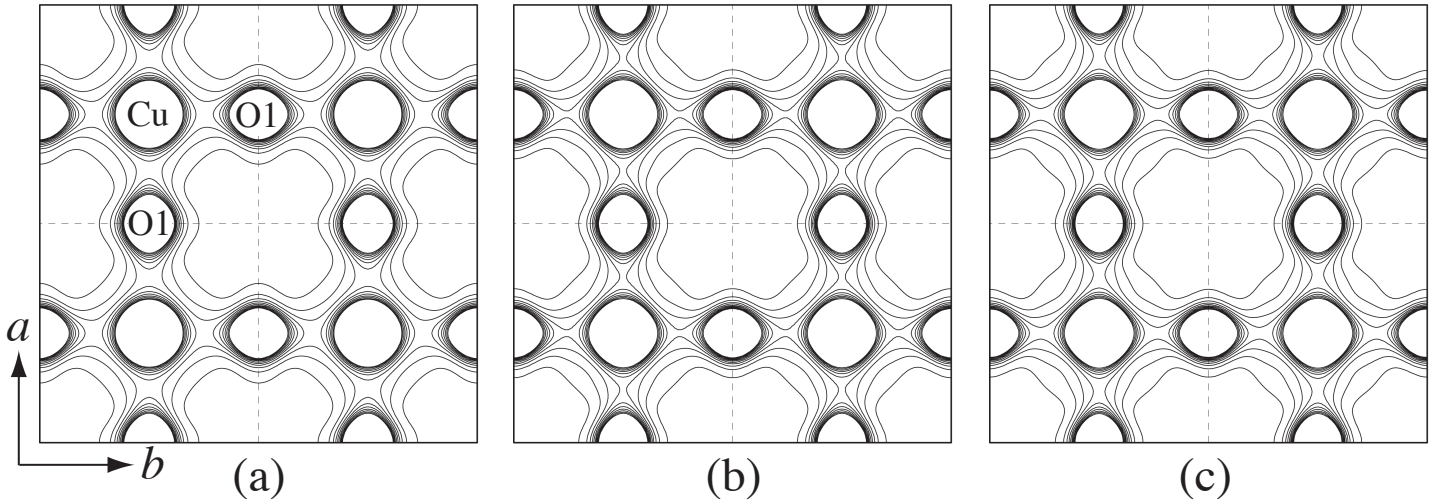


Fig. 4 Electron-density distribution on the  $\text{CuO}_2$  sheet ( $z = 1/2$  plane) in  $\text{HgBa}_2\text{CuO}_{4+\delta}$  after (a) Rietveld analysis, (b) first REMEDY cycle, and (c) second REMEDY cycle. Contours were plotted for  $0-3/\text{\AA}^3$  with a step of  $0.3/\text{\AA}^3$ .

MEM into intensity partitioning for overlapping reflections.

**Figure 5** gives (a) nuclear and (b) electron densities on the (100) plane of  $\text{HgBa}_2\text{CuO}_{4+\delta}$ . Interposition of bonding electrons between Hg and O2 and between Cu and O1 is clearly recognized in Fig. 5b. The presence of a region where electron densities are negligibly low between the Cu and O2 atoms indicates nearly electrostatic interaction between them. Comparison of Fig. 5a with Fig. 5b reveals that thermal vibrations of Cu and Hg predominate along the [001] direction perpendicular to the  $\text{CuO}_2$  sheet and on the  $z = 0$  plane perpendicular to a linear  $[\text{O2}-\text{Hg}-\text{O2}]^{2-}$  ion, respectively. These findings are reasonable considering the highly covalent character of the Cu–O1 and Hg–O2 bonds.

Though harmonic thermal motion was assumed in the Rietveld analysis prior to the REMEDY cycles, the isosurface of nuclear densities for O2 considerably deviated from an ellipsoid, as can be appreciated from Fig. 5a. In fact, the analysis of anharmonic thermal vibration [36] for O2 afforded significant cubic and quartic anharmonic terms.

Interstitial oxygen defects, O3, at  $(1/2, 1/2, 0)$  are responsible for hole doping in  $\text{HgBa}_2\text{CuO}_{4+\delta}$ . In conventional Rietveld analysis,  $B$  for a slightly occupied site like O3 is often fixed arbitrarily at a typical value,

*e.g.*,  $1 \text{\AA}^2$ , to refine only its occupancy,  $g$ , on account of very strong correlation between  $B$  and  $g$ . We took more sophisticated approaches to obtain more reliable values of  $g(\text{O3})$  and  $B(\text{O3})$ . That is,  $g(\text{O3})$  was estimated at 0.14 by integrating nuclear densities of O3, and  $B(\text{O3})$  at  $1.5 \text{\AA}^2$  by evaluating mean square displacements. The  $g(\text{O3})$  value of 0.14 corresponds to  $\delta = 0.14$ . This technique is useful for determining  $B$  and  $g$  for partially occupied sites from nuclear densities derived by MEM.

#### 8.4 Statistic distribution of H atoms in the high-temperature phase of $\text{KH}_2\text{PO}_4$

The order–disorder-type phase transition in  $\text{KH}_2\text{PO}_4$  was studied by MPF from its neutron powder diffraction data measured at room temperature and 10 K on HRPD ( $\lambda = 1.16 \text{\AA}$ ) at JRR-3M [49]. The procedure described in 3.4 was used to deal with H atoms with a negative  $b_c$  of  $-3.7390 \text{ fm}$  [2]. The ferroelectric (space group  $Fdd2$ ) and paraelectric (space group  $I\bar{4}2d$ ) phases of  $\text{KH}_2\text{PO}_4$  are stable below and above its Curie temperature,  $T_C$ , of 123 K, respectively.

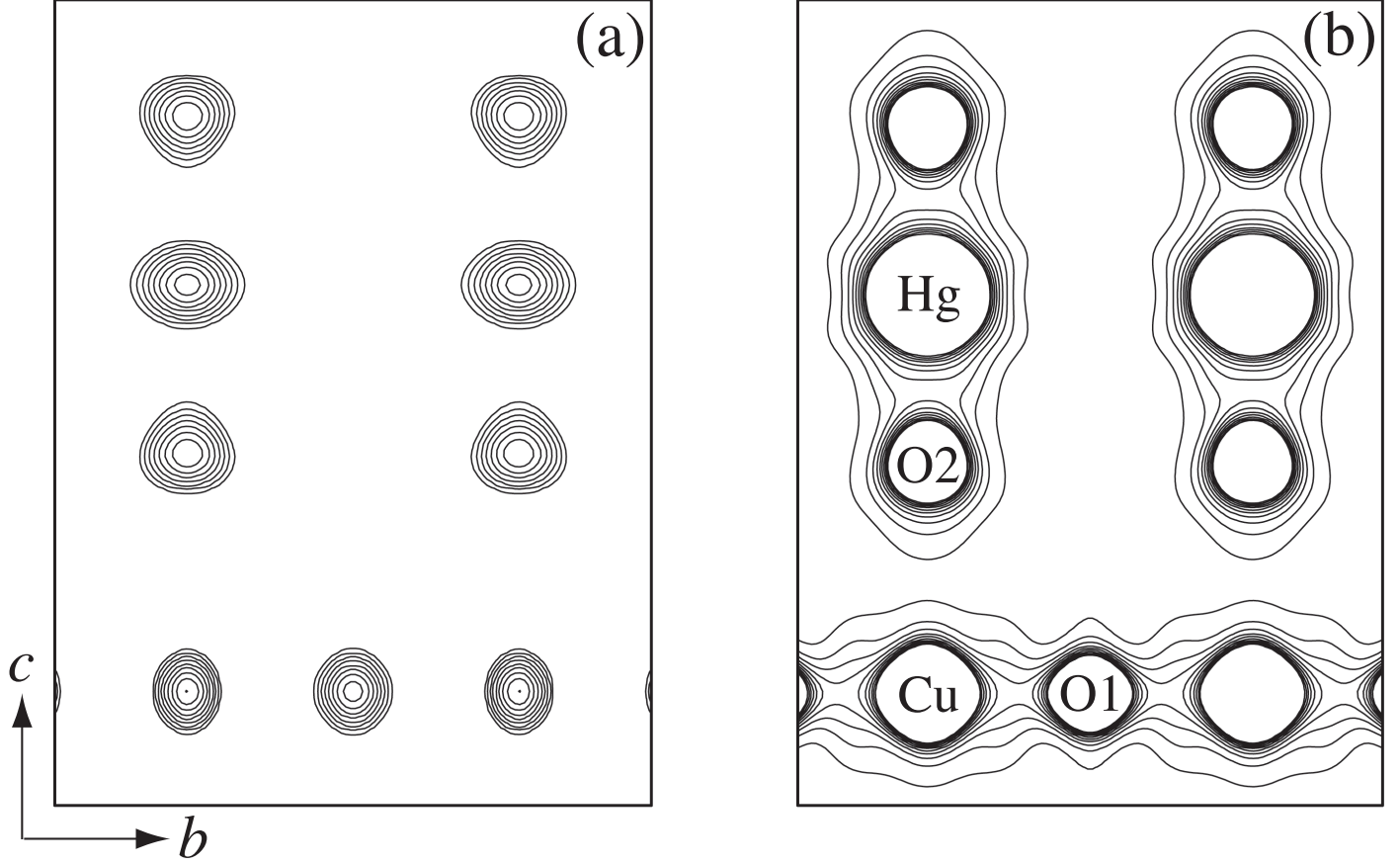


Fig. 5 (a) Nuclear- and (b) electron-density maps for the (100) plane in  $\text{HgBa}_2\text{CuO}_{4+\delta}$ . Contours were plotted for (a)  $0.1 \times 3^n \text{ fm}/\text{\AA}^3$  ( $n = 1-10$ ) and (b)  $0-3/\text{\AA}^3$  with a step of  $0.3/\text{\AA}^3$ .

In Fig. 6, nuclear densities resulting from MPF of the paraelectric phase are projected onto the (001) plane. This projection makes it possible to see the nuclear densities of all the atoms included in  $\text{KH}_2\text{PO}_4$ . H atoms are statistically situated at a pair of positions with a distance between the twin peaks of ca.  $0.36 \text{ \AA}$ , which is in good agreement with H–H distances reported in the literature. On the other hands, H atoms in the ferroelectric phase at 10 K tend to occupy a single position near to an oxygen atom. Figure 6 illustrates that the thermal vibrations of P and O atoms in the  $\text{PO}_4^{3-}$  ion are of the comparable degree but of different directional character. This finding supports the idea that the thermal vibration of the  $\text{PO}_4^{3-}$  ion is dominated by rigid-body motion, still exhibiting significant internal motion.

The MEM/Rietveld method failed in visualizing the symmetric potential valleys in the paraelectric phase, which provides evidence for the predominance

of MPF over the MEM/Rietveld method.

### 8.5 Orientational disorder of $\text{CO}_3^{2-}$ ions in $\text{Ba}_4\text{CaCu}_2\text{O}_6\text{CO}_3$

The tetragonal structure of  $\text{Ba}_4\text{CaCu}_2\text{O}_6\text{CO}_3$  (space group  $P4/mmm$ ) can be related to the perovskite-type compound  $\text{ABO}_3$  by locating larger Ba atoms at an A site and smaller Ca, Cu, and C atoms at B sites. Ca atoms and  $\text{Cu1O}_4$  squares lie on the  $z = 0$  plane, Ba and O2 atoms on the  $z = 1/4$  plane, and Cu2 ( $1b; 0, 0, 1/2$ ) and C ( $1d; 1/2, 1/2, 1/2$ ) atoms on the  $z = 1/2$  plane. Of course, three O atoms form a triangular  $\text{CO}_3^{2-}$  ion with the C atom at its center.

Rietveld analysis from neutron powder diffraction data measured at room temperature [50] showed that one O3 atom is split into four pieces to occupy a  $4k$  site on a line connecting C and Cu2 atoms. However, the static orientational disorder of  $\text{CO}_3^{2-}$  ions is so

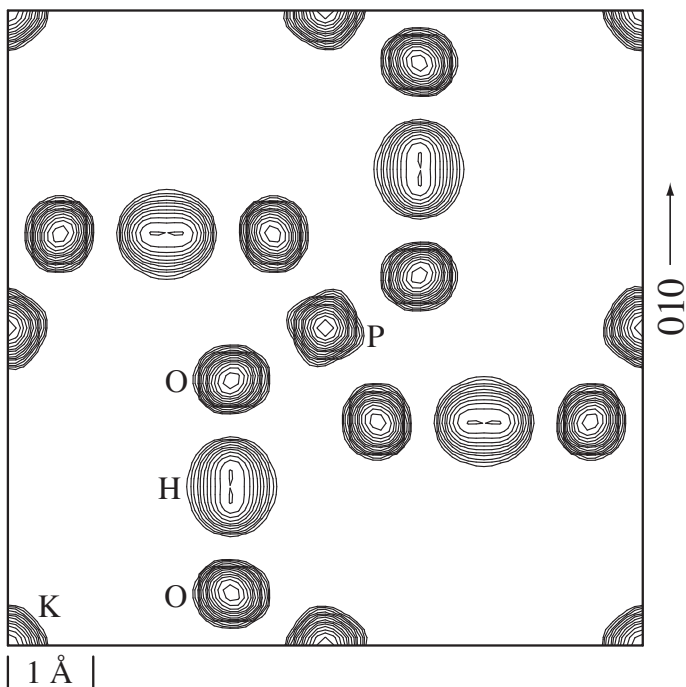


Fig. 6 Nuclear-density distribution projected on the (001) plane in the paraelectric phase of  $\text{KH}_2\text{PO}_4$  at room temperature. Contours were plotted for  $2.5 \times 1.5^n \text{ fm}/\text{\AA}^3$  ( $n = 0 - 20$ ).

pronounced that positions of remaining two O4 atoms could not be determined unambiguously.

We have recently reanalyzed neutron powder diffraction data measured on the BT-1 diffractometer at NIST by MPF and successfully visualized what was overlooked in the previous Rietveld analysis (**Fig. 7**) [51]. MPF decreased  $R_{\text{wp}}$  ( $S$ ),  $R_p$ ,  $R_B$ , and  $R_F$  from 5.17 % (1.32), 4.14 %, 5.59 %, and 3.05 % in the final Rietveld analysis to 4.26 % (1.08), 3.46 %, 2.35 %, and 1.78 %, respectively.

In addition to O3 and O4 ( $2h$ ;  $1/2$ ,  $1/2$ ,  $z$ ;  $z \approx 0.43$ ) atoms distant from the  $1d$  site by *ca.* 1.29 Å, we found four positions apart from the  $1d$  site by *ca.* 1.85 Å along the  $[110]$  direction (Fig. 7a). Because 1.85 Å corresponds to a Cu–O bond length, Cu3 atoms are believed to substitute for part of C atoms at  $1d$ . Four O5 atoms to which each Cu3 atom at  $1d$  is coordinated are clearly visualized by MEM. In Fig. 7b, peaks for O5 are much higher than those for O3, which is explained in terms of high densities of O3 nuclei in the space excluding the  $z = 1/2$  plane. The content of O3 is much higher than that of O5 as

a whole. Thus, MPF released us from the preconception that C fully occupies the  $1d$  site.

### 8.6 Dynamic disorder of $\text{Cu}^+$ ions in a superionic conductor $\text{Rb}_4\text{Cu}_{16}\text{I}_{7.2}\text{Cl}_{12.8}$

The conductivity of  $\text{Rb}_4\text{Cu}_{16}\text{I}_7\text{Cl}_{13}$  (space group  $P4_132$ ) at room temperature is  $0.34 \text{ S cm}^{-1}$ , which is the highest of all the superionic conductors. Its structure changes without any phase transitions from a low-temperature phase where  $\text{Cu}^+$  ions hardly migrate to the high ionic conductor because lattice defects are generated by thermal excitation. **Figure 8** illustrates results of MPF structure refinements for  $\text{Rb}_4\text{Cu}_{16}\text{I}_{7.2}\text{Cl}_{12.8}$  at 11 K and 280 K from neutron powder diffraction data measured on the HB-4 diffractometer at HFIR [34]. In the case of the data taken at 280 K, two REMEDY cycles lowered  $R_{\text{wp}}$  ( $S$ ) from 6.06 % (1.05) to 5.98 % (1.03) and  $R_B$  from 6.25 % to 5.18 %.

The most significant difference between Figs. 8a and 8b is that  $\text{Cu}^+$  ions are localized at definite positions at 11 K but delocalized spirally at room temperature.  $\text{Rb}_4\text{Cu}_{16}\text{I}_7\text{Cl}_{13}$  has three Cu sites in the asymmetric unit: Cu1 and Cu2 at  $24e$  and Cu3 at  $8c$ . From Fig. 8b, we confirmed that  $[\text{Cu1}-\text{Cu2}-]_{\infty}$  chains are main conduction pathways in this material, as previously suggested from Rietveld analysis of time-of-flight neutron powder diffraction data [35]. Visualization of distribution of  $\text{Cu}^+$  ions in the unit cell with VEND is very useful to understand the positional disorder in this system three-dimensionally, as can be appreciated from Fig. 8.

### 8.7 Positional and orientational disorder in a solid solution of $\text{Sr}_{9.3}\text{Ni}_{1.2}(\text{PO}_4)_7$

To apply MPF to high-resolution powder diffraction data, we measured synchrotron X-ray powder diffraction data on a powder diffractometer (beam line BL15XU at SPring-8) with the Debye–Scherrer geometry using capillary tubes rotated at a speed of 6.3 rad/s. Incident beams from an undulator were monochromatized with inclined double-crystal monochromators of Si(111). An instrumental resolution at the top international level is attained in this diffractometer.

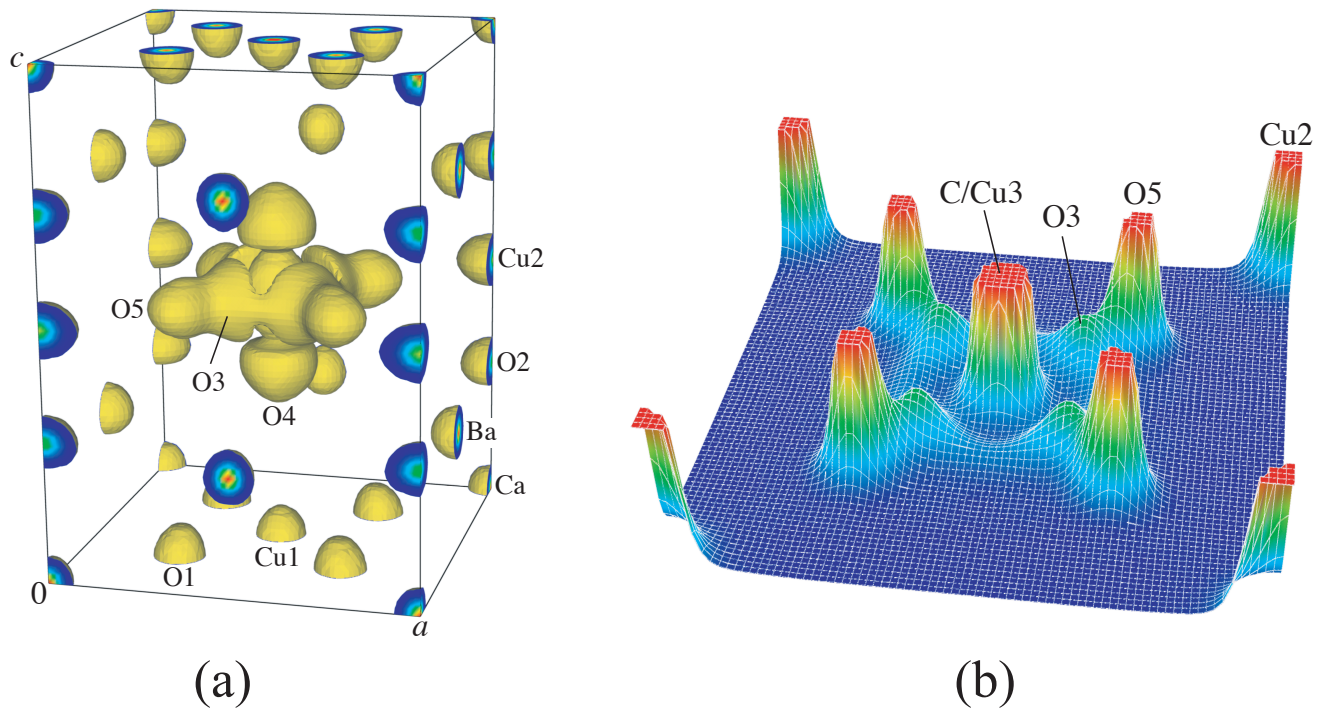


Fig. 7 (a) Isosurfaces of nuclear densities at a  $0.6 \text{ fm}/\text{\AA}^3$  level and (b) a bird's eye view of nuclear densities up to 8 % of the maximum ( $663.9 \text{ fm}/\text{\AA}^3$ ) on the  $z = 1/2$  plane in  $\text{Ba}_4\text{CaCu}_2\text{O}_6\text{CO}_3$ .

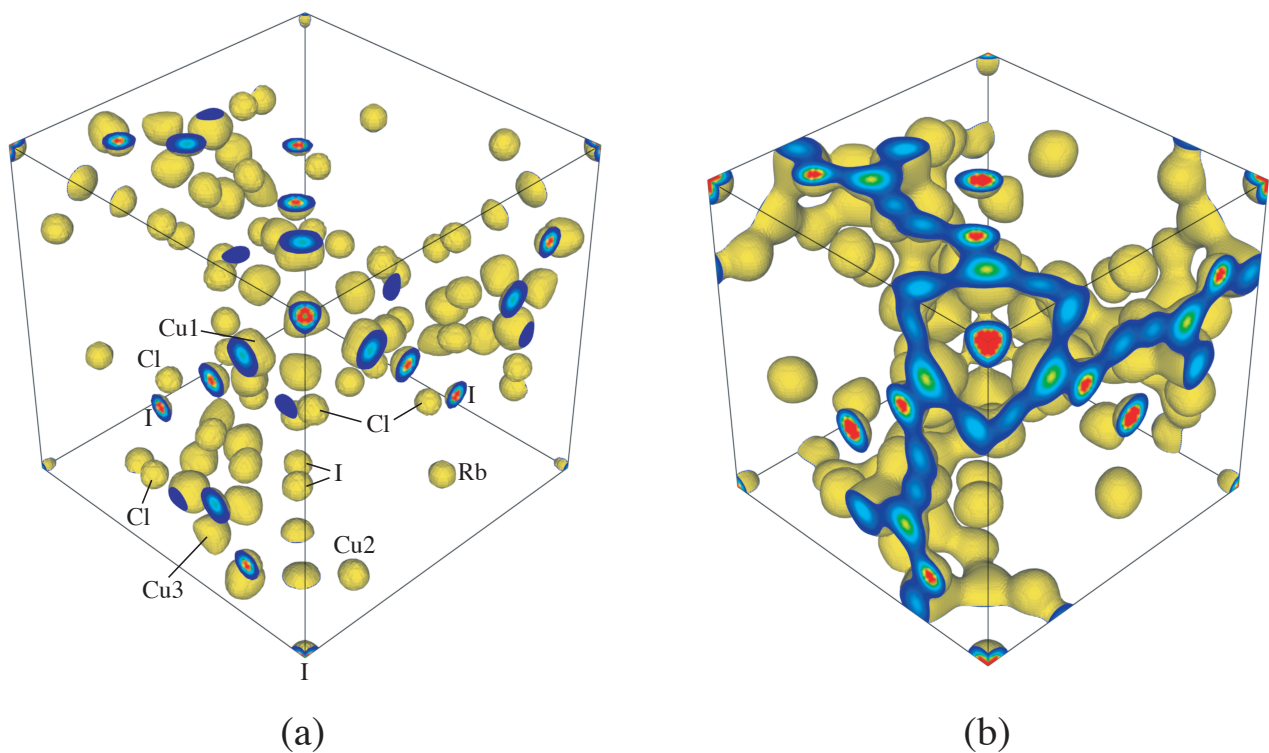


Fig. 8 Isosurfaces of nuclear densities in  $\text{Rb}_4\text{Cu}_{16}\text{I}_{7.2}\text{Cl}_{12.8}$  at (a) 11 K and (b) 280 K. Equidensity level:  $0.2 \text{ fm}/\text{\AA}^3$ . In (b), sections at unit-cell edges clearly display  $[\text{Cu1}-\text{Cu2}]_\infty$  pathways.

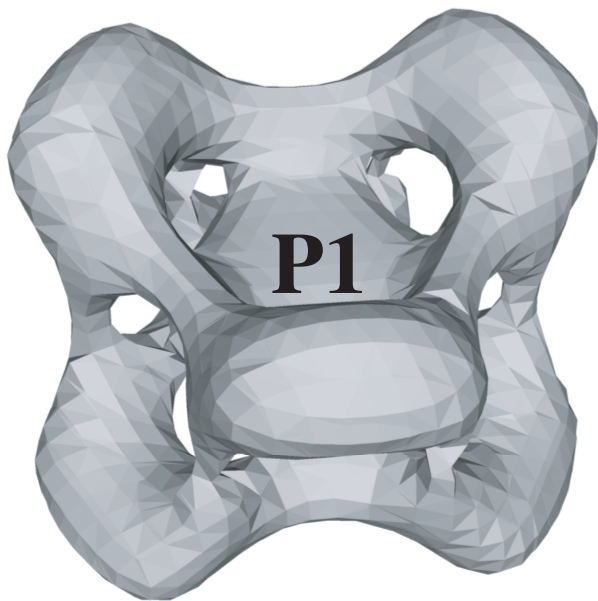


Fig. 9 Three-dimensional electron-density image of a  $\text{P1O}_4^{3-}$  ion in  $\text{Sr}_{9.3}\text{Ni}_{1.2}(\text{PO}_4)_7$  with an equidensity level of  $1.6/\text{\AA}^3$ .

X-Ray powder diffraction data of a whitlockite-like phosphate,  $\text{Sr}_{9.3}\text{Ni}_{1.2}(\text{PO}_4)_7$  (space group  $R\bar{3}m$ ) [32], were taken at 100 K with a wavelength of 0.8000  $\text{\AA}$  and a Ge(111) analyzer. Very sharp profiles were observed with FWHM's ranging from  $0.008^\circ$  to  $0.019^\circ$ . In  $\text{Sr}_{9.3}\text{Ni}_{1.2}(\text{PO}_4)_7$ , part of  $\text{Sr}^{2+}$  and  $\text{PO}_4^{3-}$  ions exhibit highly disordered arrangements. Then, we found positions of these atoms by the MEM/Rietveld method, building a split-atoms model. Subsequent two REMEDY cycles decreased  $R_{\text{wp}}(S)$ ,  $R_{\text{p}}$ ,  $R_{\text{B}}$ , and  $R_{\text{F}}$  a great deal from 5.39 % (2.30), 3.93 %, 2.80 %, and 1.88 %, in the final Rietveld refinement adopting the split-atom model to 5.18 % (2.20), 3.71 %, 1.03 %, and 0.82 %, respectively. As usual,  $R_{\text{B}}$  and  $R_{\text{F}}$  dropped dramatically in the first cycle. **Figure 9** illustrates isosurfaces of electron densities determined by MPF for  $\text{P1O}_4$  tetrahedron. This figure revealed that such pronounced orientational disorder can hardly be represented with the split-atom model, which is the main reason why MPF lowered the  $R$  factors surprisingly. MPF afforded an excellent fit between observed and calculated patterns (**Fig. 10**).

These results proved that the MPF method is effective even in the structure refinement from the ultrahigh-resolution X-ray diffraction data.

## 8.8 Structure refinement of LTL by MPF

A dehydrated zeolite, Linde Type L (LTL,  $\text{K}_9\text{Al}_9\text{Si}_{27}\text{O}_{72}$ , space group  $P6/mmm$ ) [52], is a microporous material with a disordered structure including large one-dimensional channels parallel to the  $c$  axis. Its synchrotron X-ray powder diffraction data ( $\lambda = 1.2000 \text{\AA}$ ) were collected at room temperature with the Ge(111) analyzer.  $R_{\text{wp}}(S)$ ,  $R_{\text{p}}$ ,  $R_{\text{B}}$ , and  $R_{\text{F}}$  were respectively 4.90 % (2.47), 3.19 %, 1.60 %, and 1.59 % in the final Rietveld refinement and 4.46 % (2.24), 2.93 %, 0.69 %, and 0.84 % after two REMEDY cycles. **Figure 11** shows the final profile fit to be very excellent. Electron-density images clearly showed a framework consisting of highly covalent (Si,Al)–O bonds. We also found that electron-density distribution around  $\text{K}^+$  ions incorporated in the framework is not spherical but anisotropic.

## 9. CLOSING REMARKS

The revolutionary MPF technology was devised to overcome limitations of Rietveld analysis. RIETAN-2000 is distinguished from other programs for classical Rietveld analysis by this elegant methodology. In MPF, electron/nuclear-density distribution changes noticeably with accompanying decreases in  $R_{\text{B}}$  and  $R_{\text{F}}$  during REMEDY cycles, which is a strong piece of evidence for the reduction in the bias of the structural model and the serious flaw of the MEM/Rietveld method on its use to determine electron/nuclear densities [3, 4].

MEM is, *per se*, model-free whereas the MEM/Rietveld method is more or less model-dependent. The MEM/Rietveld method should never be confounded with MEM. This expedient method is, therefore, unsound on its application to determination of electron/nuclear-density distribution though it is certainly effective for the rough visualization of electron/nuclear densities just after Rietveld analysis. We agree that the MEM/Rietveld method is more effective in modifying imperfect structural models than Fourier/D synthesis thanks to higher S/N ratios due to estimation of structure factors for unobserved reflections and non-negative densities obtained by MEM. However, it cannot give accurate 3D densities particularly when reflections heavily overlap

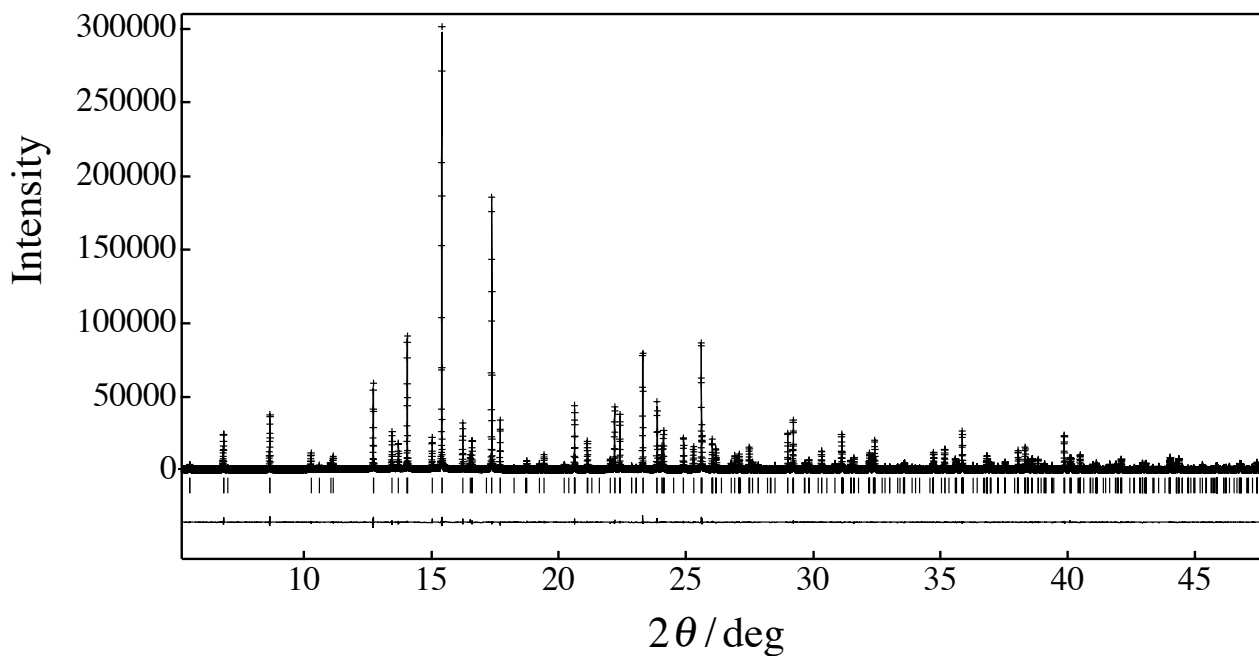


Fig. 10 Observed (+ symbols), calculated (upper solid line), and difference (lower solid line) patterns resulting from the final MPF structure refinement from the synchrotron X-ray powder diffraction data for  $\text{Sr}_{9.3}\text{Ni}_{1.2}(\text{PO}_4)_7$ . Tick marks denote the peak positions of possible Bragg reflections.

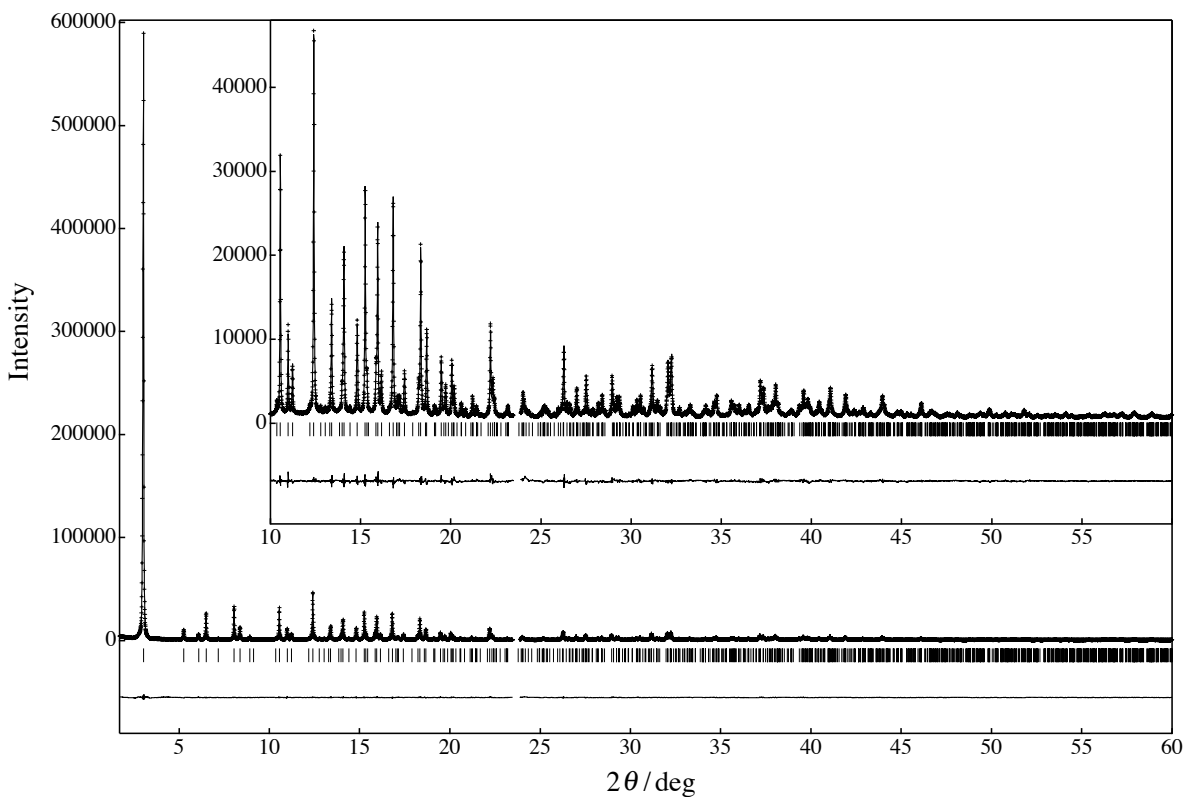


Fig. 11 Observed, calculated, and difference patterns resulting from the final MPF structure refinement from the synchrotron X-ray powder diffraction data for LTL. The patterns between  $10^\circ$  and  $60^\circ$  are magnified in the inset.

with each other because of low symmetry and insufficient instrumental resolution. Frankly speaking, the MEM/Rietveld method is nothing but iterative conventional Rietveld refinements where structural models are modified, if necessary, after visualizing electron/nuclear densities by MEM.

The number of REMEDY cycles required for convergence generally increases with lowering resolution in a diffraction pattern because observed intensities of Bragg reflections are repartitioned with  $F_c(\text{MEM})$  calculated from  $F_o(\text{Rietveld})$  or  $F_o(\text{w.p.f.})$ . Even with high-resolution synchrotron X-ray powder diffraction data, at least one cycle of MPF proved to be indispensable for the determination of more accurate electron densities. In MPF, parameters other than structure parameters are refined, and partition of observed intensities is rapidly improved because of the use of  $F_c(\text{MEM})$ . The MPF method is, hence, so much superior to the MEM/Rietveld method, where the analytical method in the Fourier synthesis of  $F_o(\text{Rietveld})$  data is merely replaced with MEM. From the amazing results presented above for the several materials, we conclude MPF to be a powerful method of structure refinement where imperfect structural representations in conventional Rietveld analysis are supplemented with model-free MEM.

## ACKNOWLEDGMENTS

The technology of MPF owes its existence to Shintaro Kumazawa's proposal to implement it in RIETAN-2000. The development of both RIETAN-2000 and VENUS was financially supported by the Project for Superconductivity Research at NIMS.

## References

- [1] Sakata, M., Mori, R., Kumazawa, S., Takata, M., Toraya, H. 1990, *J. Appl. Crystallogr.* **23**, 526.
- [2] Sears, V.F. 1999, *International Tables for Crystallography*, Vol. C, 2nd ed., A.J.C. Wilson, E. Prince (Eds.), Kluwer Academic Publishers, Dordrecht, pp. 440–450.
- [3] Takata, M., Umeda, B., Nishibori, E., Sakata, M., Saito, Y., Ohno, M., Shinohara, H. 1995, *Nature (London)* **377**, 46.
- [4] Takata, M., Nishibori, E., Sakata, M. 2001, *Z. Kristallogr.* **216**, 71.
- [5] Rietveld, H.M. 1969, *J. Appl. Crystallogr.* **2**, 65.
- [6] McCusker, L.B., Von Dreele, R.B., Cox, D.E., Louër, D., Scardi, P. 1999, *J. Appl. Crystallogr.* **32**, 36.
- [7] Izumi, F., Kumazawa, S., Ikeda, T., Ida, T. 1998, *Powder Diffraction*, Proc. Int. School Powder Diffr. (ISPD'98), S.P. Sen Gupta (Ed.), Allied Publishers, New Delhi, pp. 24–36.
- [8] Izumi, F. 2000, *Rigaku J.* **17**, No. 1, 34.
- [9] Izumi, F., Kumazawa, S., Ikeda, T., Hu, W.-Z., Yamamoto, A., Oikawa, K. 2001, *Mater. Sci. Forum* **378–381**, 59.
- [10] Izumi, F., Ikeda, T. 2001, *Commission on Powder Diffraction*, IUCr, Newslett. No. 26, 7.
- [11] Izumi, F., Ikeda, T. 2000, *Mater. Sci. Forum* **321–324**, 198.
- [12] Dilanian, R.A., Izumi, F. 2003, unpublished work.
- [13] Kumazawa, S., Kubota, Y., Takata, M., Sakata, M., Ishibashi, Y. 1993, *J. Appl. Crystallogr.* **26**, 453.
- [14] Dilanian, R.A., Izumi, F. 2002, unpublished work.
- [15] Gull, S.F., Daniel, G.J. 1978, *Nature (London)* **272**, 686.
- [16] Collins, D.M. 1982, *Nature (London)* **298**, 49.
- [17] Bricogne, G. 1988, *Acta Crystallogr., Sect. A* **44**, 517.
- [18] Jaynes, E.T. 1957, *Phys. Rev.* **106**, 620.
- [19] Kumazawa, S., Takata, M., Sakata, M. 1995, *Acta Crystallogr., Sect. A* **51**, 47.
- [20] Wilkins, S.W., Varghese, J.N., Lehmann, M.S. 1983, *Acta Crystallogr., Sect. A* **39**, 47.
- [21] Sakata, M., Uno, T., Takata, M. 1993, *J. Appl. Crystallogr.* **26**, 159.
- [22] Burger, K. 1998, MEND available for download from <http://www.uni-tuebingen.de/uni/pki/maxent/maxent.html>.
- [23] Tanaka, H., Takata, M., Nishibori, E., Kato, K., Iishi, T., Sakata, M. 2002, *J. Appl. Crystallogr.* **35**, 282.
- [24] Hahn, Th. (Ed.) 2002, *International Tables for Crystallography*, Vol. A, 5th ed., Kluwer Academic Publishers, Dordrecht, Part 7.

- [25] Eyck, L.F.T. 1973, *Acta Crystallogr., Sect. A* **29**, 183.
- [26] Rowicka, M., Kudlicki, A., Otwinowski, Z. 2002, *Acta Crystallogr., Sect. A* **58**, 574.
- [27] Toraya, H. 1995, *The Rietveld Method*, R.A. Young (Ed.), Oxford University Press, Oxford, Chap. 14.
- [28] Pawley, G.S. 1981, *J. Appl. Crystallogr.* **14**, 357.
- [29] Le Bail, A., Duroy, H., Fourquet, J.L. 1988, *Mater. Res. Bull.* **23**, 447.
- [30] Ikeda, T., Izumi, F., Kodaira, T., Kamiyama, T. 1998, *Chem. Mater.* **10**, 3996.
- [31] Ikeda, T., Akiyama, Y., Izumi, F., Kiyozumi, Y., Mizukami, F., Kodaira, T. 2001, *Chem. Mater.* **13**, 1286.
- [32] Belik, A.A., Izumi, F., Ikeda, T., Morozov, V.A., Dilanian, R.A., Torii, S., Kopnin, E.M., Lebedev, O.I., Van Tendeloo, G., Lazoryak, B.I. 2002, *Chem. Mater.* **14**, 4464.
- [33] Takada, K., Sakurai, H., Takayama-Muromachi, E., Izumi, F., Dilanian, R.A., Sasaki, T. 2003, *Nature (London)* **422**, 53.
- [34] Oikawa, K., Kamiyama, T., Kannno, R., Izumi, F., Ikeda, T., Chakoumakos, B.C. *Mater. Sci. Forum*, in press.
- [35] Kanno, R., Ohno, K., Kawamoto, Y., Takeda, Y., Yamamoto, O., Kamiyama, T., Asano, H., Izumi, F., Kondo, S. 1993, *J. Solid State Chem.* **102**, 79.
- [36] Kumazawa, S., Takata, M., Sakata, M. 1995, *Acta Crystallogr., Sect. A* **51**, 651.
- [37] Frisch, Æ., Frisch, M.J. 1999, *Gaussian 98 User's Reference*, 2nd ed., Gaussian, Inc., Pittsburgh.
- [38] Adachi, H., Tsukada, M., Satoko, C. 1978, *J. Phys. Soc. Jpn.* **45**, 875.
- [39] Blaha, P., Schwarz, K., Madsen, G., Kvasnicka, D., Luitz, J. 2001, *WIEN2k, an Augmented Plane Wave + Local Orbitals Program for Calculating Crystal Properties*, K. Schwarz (Ed.), Technische Universität Wien, Wien.
- [40] Palatinus, L., van Smaalen, S. 2002, *Acta Crystallogr., Sect. A* **58**, 559.
- [41] Sasaki, T., Kooli, F., Iida, M., Michiue, Y., Takenouchi, S., Yajima, Y., Izumi, F., Watanabe, M., Chakoumakos, B.C. 1998, *Chem. Mater.* **10**, 4123.
- [42] Izumi, F., Ikeda, T., Sasaki, T., Kumazawa, S. 2000, *Mol. Cryst. Liq. Cryst.* **341**, 253.
- [43] Young, R.A. 1995, *The Rietveld Method*, R.A. Young (Ed.), Oxford University Press, Oxford, Chap. 1.
- [44] Nozue, Y., Kodaira, T., Goto, T. 1992, *Phys. Rev. Lett.* **68**, 3789.
- [45] Ikeda, T., Kodaira, T., Izumi, F., Kumazawa, S. 2000, *Mol. Cryst. Liq. Cryst.* **341**, 447.
- [46] Ikeda, T., Kodaira, T., Izumi, F., Kamiyama, T., Ohshima, K. 2000, *Chem. Phys. Lett.* **318**, 93.
- [47] Yamamoto, A., Hu, W.-Z., Izumi, F., Tajima, S. 2001, *Physica C (Amsterdam)* **351**, 329.
- [48] Izumi, F., Yamamoto, A., Khasanova, N.R., Kumazawa, S., Hu, W.-Z., Kamiyama, T. 2000, *Physica C (Amsterdam)* **335**, 239.
- [49] Kumazawa, S., Yamamura, S., Nishibori, E., Takata, M., Sakata, M., Izumi, F., Ishii, Y. 1999, *J. Phys. Chem. Solids* **60**, 1407.
- [50] Kikuchi, M., Izumi, F., Kikuchi, M., Ohshima, E., Morii, Y., Shimojo, Y., Syono, Y. 1995, *Physica C (Amsterdam)* **247**, 183.
- [51] Dilanian, R.A. *et al.*, unpublished work.
- [52] Barrer, R.M., Villiger, H. 1969, *Z. Kristallogr.* **128**, 352.